Physica D 483 (2025) 134986

Contents lists available at ScienceDirect

Physica D

journal homepage: www.elsevier.com/locate/physd

An extended corrosive-passivating model with cross-diffusion for the initiation of corrosion patterns☆

Giancarlo Consolo [a],*, Guglielmo Inferrera [a], Edoardo Proverbio [b], Cinzia Soresina [c]

[a] Department of Mathematical, Computer, Physical and Earth Sciences, University of Messina, Italy
[b] Department of Engineering, University of Messina, Italy
[c] Department of Mathematics, University of Trento, Italy

ARTICLE INFO

Communicated by Dmitry Pelinovsky

Keywords:
Pattern formation
Multiple scales
Fast-reaction limit
Cross-diffusion
Activator–inhibitor dynamics

ABSTRACT

An extended version of the Barkley model is proposed to elucidate the process of initiation of localized corrosion patterns observed on metal surfaces, in particular on the bottom of fuel tanks. The model describes the interaction between a fast activator variable, the surface concentration of the corrosive species, and a slow inhibitor, the surface concentration of the passivating one, which was assumed to be diffusionless in its original formulation. By exploiting the dichotomy between different states of the passivating species occurring at a faster time scale, the fast-reaction limit yields a novel corrosive-passivating model including a cross-diffusion term for the passivating species. When the cross-diffusion coefficient exceeds a given threshold, the cross-diffusion term so deduced allows the destabilization of the homogeneous steady-state to spatial disturbances, triggering corrosion Turing patterns. The study is complemented by numerical investigations carried out over 1D and 2D domains. These are used to corroborate analytical predictions and to provide additional insights into the morphology of the emerging corrosion patterns. Indeed, by means of a suitable choice of model parameters and initial conditions, a qualitative agreement with some experimental data showing the presence of isolated or merged corrosion "pits" is achieved. Results suggest that the extended model proposed here might be useful to improve the predictive tools currently employed in the maintenance strategies of metal surfaces.

1. Introduction

Corrosion is the degradation of a metal alloy caused by electrochemical reactions with its surrounding environment [1]. Corrosion manifests in various forms, including galvanic, uniform, and localized, among others. Here, focus is given on the localized corrosion which takes place at discrete sites on a metal surface and can lead to the development of several structural defects in the form of stripes [2,3] or pits [4–6]. Stripe-like patterns (also termed tiger stripes or B-stripes) manifest themselves in the form of parallel bands and have been observed, for instance, in additively manufactured stainless steel [5]. On the other hand, pitting corrosion patterns are characterized by the creation of localized attacks on the surface of the metal alloy and can be observed in several environments, especially on the bottom of atmospheric fuel storage tanks. In particular, initially, each pit forms independently, often originating from imperfections or weak points on the material's surface. However, when the pits are extremely close to each other, they may interact and form a unique larger cluster. This structure creates a concentration gradient around itself, encouraging a continuous flow of corrosive species towards its interior. Additionally, the local electric potential becomes concentrated around the pits, accelerating the anodic reaction. As a result, the pit depth grows over time, posing a significant structural risk to the material, an issue particularly relevant in systems exposed to extreme conditions, such as marine environments and corrosive fuels. Understanding and modelling this process, as well as predicting the time evolution of pits, becomes thus essential for predicting the so-called "residual useful lifetime" of fuel tanks and for developing effective protection strategies. Indeed, green industries and refineries are currently facing growing challenges related to the susceptibility of atmospheric storage tanks to such a phenomenon of localized corrosion, mainly due to the higher aggressivity of biofuels in comparison with traditional fuels [7–10]. In addition, the integrity check of fuel tanks is generally carried out by periodic inspections (typically every 10 years or more) of the thickness of the bottom sections after having emptied the container and stopped the plant [11]. Apart from the economic burden connected to this activity, the maximum corrosion depth of the bottom of storage tanks cannot

☆ This article is part of a Special issue entitled: 'Multiple Scales' published in Physica D.

* Corresponding author.
E-mail address: gconsolo@unime.it (G. Consolo).

https://doi.org/10.1016/j.physd.2025.134986
Received 7 July 2025; Received in revised form 10 October 2025; Accepted 16 October 2025
Available online 20 October 2025

be exactly determined by discrete thickness measurements, especially in the presence of multiple corrosion pits. Therefore, to ensure the reliability of such metal surfaces and prevent potential leaks, several predictive tools, capable of providing a quantitative estimation of the corrosion rate as a function of the environmental parameters here involved, have been currently developing and constitute an intense area of research [7,12–18],

In the literature, mathematical models of corrosion typically rely on Poisson–Nernst–Planck systems, where each Nernst–Planck equation describes the mass balance of each chemical ionic species present in the electrolyte solution, while the Poisson one rules the spatial distribution of the electrostatic potential [7,13–16,18]. These equations are crucial for understanding ion transport in electrochemical systems, offering insights into the concentration gradients that drive corrosion processes. To avoid the complexities associated with the need to explicitly track moving boundaries (i.e., the electrolyte/metal interface, as it happens during the spatio-temporal evolution of corrosion pits), an alternative approach involves the so-called phase-field models. In this case, the spatio-temporal evolution of the metal/liquid interface is tracked by means of an auxiliary order parameter that undergoes a smooth variation between the two phases [7,13,14,18]. However, owing to the complexity of these nonlinear and coupled equations, the solution is typically obtained numerically, and not much information, such as the existence of activation thresholds, may be retrieved by analytical calculations. In addition, the above-mentioned models constitute very useful and accurate tools for the characterization of the factors influencing pit growth, but rely on the common assumption that the pit initiation stage has already been concluded. In other words, not much modelling effort on the mechanisms leading to the initiation of corrosion patterns was made.

This work is an attempt to fill this gap as it aims at proposing a possible mechanism, based upon cross-diffusion effects, through which corrosion patterns may originate on a metal surface. In particular, the goal is to develop a mathematical model presenting diffusion-driven Turing instability [19], responsible for the onset of spatial patterns. As known, the mechanism of Turing instability, initially studied in biological contexts to explain pattern formation in nature, is nowadays finding applications in many areas [19–26]. In the context of corrosion, the occurrence of Turing instability implies that the diffusion of reactive chemical species, such as metal ions and oxygen, interacts nonlinearly with local electrochemical reactions. This leads to the formation of spatial patterns of different morphologies on the material's surface, which manifest themselves as localized concentrations of the corrosive species.

The starting point of this investigation is the so-called Barkley model, a well-known prototype of the two-variable system of reaction–diffusion equations used to describe the propagation of waves, such as stable or modulated spiral waves, in excitable media [27,28]. This model has also been applied in the context of cardiac arrhythmia [29], tumour growth [30], and, quite recently, even in the context of corrosion [31]. In this latter case, the Barkley model includes the dynamics of a fast activator variable, that approximates the surface concentration of the corrosive species, and a slow control variable, that represents the surface recovery or passivating species and is used to trace the electrochemical dynamics at the moving interface between electrolyte solution and the metal surface. However, since the slow control variable is assumed to be diffusionless, the conditions for the occurrence of diffusion-driven Turing instability [19] cannot be met.

To overcome this issue and propose a more accurate description of the localized corrosion process, the phenomenon is investigated in more detail at the so-called *mesoscopic* scale, namely a scale lying in between the *microscopic* (individual) level and the *macroscopic* level (total species concentrations). In particular, the passivating species is subdivided into two different states, and the transition processes occurring at a faster time scale are taken into account. At *macroscopic* scale (i.e., the scale at which the only total concentration of the passivating species is considered and the fast-processes are at a quasi-steady state), this approach will lead to an extended corrosive-passivating model where a cross-diffusion term incorporates the fast-reaction processes.

This approach, based on dichotomy and time-scale arguments, has been used in other contexts to obtain cross-diffusion systems as the singular limit of fast-reaction systems [32–38]. Noteworthy, the presence of a cross-diffusion term in the model equations will be justified here even in the context of metal surface corrosion. As the linearized analysis will reveal, this additional contribution constitutes the key factor to trigger the initiation of localized corrosion patterns.

The importance of studying this phenomenon lies in its ability to explain why, under certain environmental conditions, well-defined corrosion patterns emerge on a metal surface, instead of a uniform degradation. Understanding how Turing instabilities influence metal corrosion can guide the development of more corrosion-resistant materials and more effective mitigation strategies. For instance, altering the material composition or the chemical environment could prevent such instabilities from occurring, thus reducing damages.

The paper is organized as follows. In Section 2, the original Barkley model is presented. Then, its equilibria are computed, their local stability properties against homogeneous perturbations are analysed, and the existence of positively invariant regions is proved. In Section 3, motivated by the impossibility of generating Turing patterns about these equilibria, the underlying chemical processes are investigated in more detail, formulating the fast-reaction system and its fast-reaction limit. This will lead to the formulation of an extended version of the Barkley model including cross-diffusion effects. In Section 4, Turing stability analysis is performed to define the conditions under which cross-diffusion-driven instability takes place. In such an analysis, the critical value for the wavenumber and bifurcation parameter, here taken as the coefficient of cross-diffusion for the passivating species, will be deduced. In Section 5, the numerical schemes used to numerically integrate the governing system in both 1D and 2D domains are sketched. Section 6 is entirely devoted to numerical investigations with a twofold aim: on the one side, to corroborate analytical predictions and, on the other side, to qualitatively mimic the results of experimental data. In the last Section 7, we provide some final remarks on the results obtained here and propose possible extensions of the present work.

2. The original Barkley model

A two-compartment model of localized corrosion can be built starting from the original Barkley model [27,28,31]. It is an activator–inhibitor model describing the excitable behaviour of a fast activator variable u, representing the surface concentration of the corrosive species, and a slow control variable v, mimicking the surface concentration of the recovery species playing the role of passivating. The dimensionless model reads:

$$\begin{aligned} &\frac{\partial u}{\partial t} - D_{11}\Delta u = \delta^{-1} u(1-u)\left(u - \frac{v+b}{a}\right) = f(u,v), \\ &\frac{\partial v}{\partial t} = u - v = g(u,v). \end{aligned} \tag{1}$$

Here, the parameter δ provides the ratio of reaction time scales, and is taken to be small to mimic the fast dynamics of corrosive species in comparison with the slow ones associated with the passivating species; whereas a and b are positive parameters defining the so-called excitability threshold $u_{th} = (v+b)/a$. According to this model, the species u undergoes a standard diffusion with coefficient D_{11}, while the inhibitor v is taken to be diffusionless.

Let us investigate, first, the spatially-homogeneous dynamics governed by:

$$\begin{aligned} &\frac{\mathrm{d}u}{\mathrm{d}t} = f(u,v), \\ &\frac{\mathrm{d}v}{\mathrm{d}t} = g(u,v). \end{aligned} \tag{2}$$

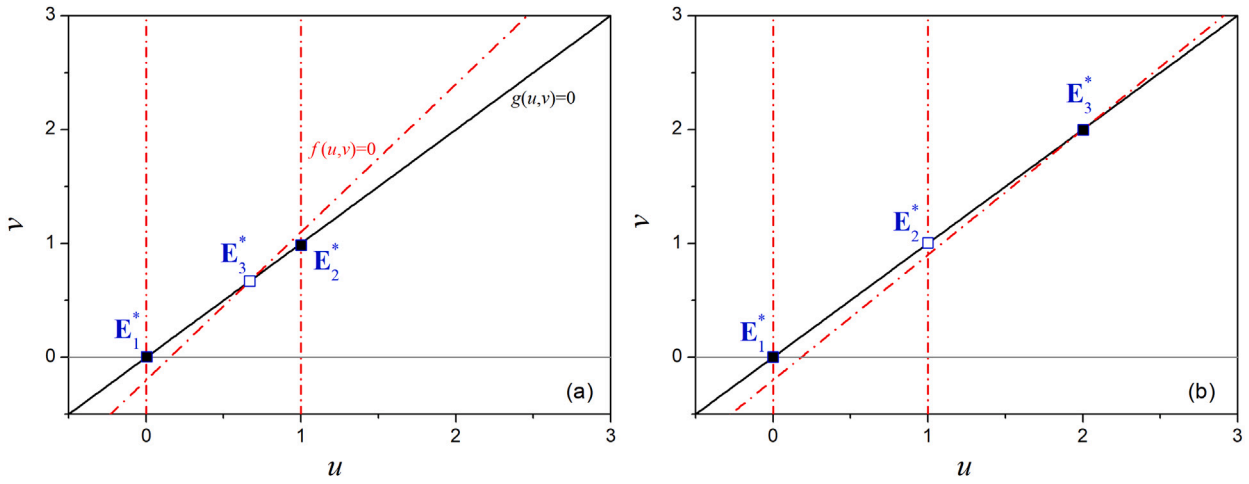

Fig. 1. Nullclines of the dynamical system (2): (a) $a = 1.3$, $b = 0.2$, representative of the condition $a > 1 + b$; (b) $a = 1.1$, $b = 0.2$, representative of $1 < a < 1 + b$. Red dashed–dotted lines represent the u–nullcline which factorizes into $u = 0$, $u = 1$ and $u = u_{th} = (v + b)/a$, whereas the black solid line denotes the v– nullcline. Solid and empty squares denote stable and unstable steady states, respectively.

By denoting the vector of state variables by $\mathbf{E} = (u, v)$, the previous system admits three equilibria $\mathbf{E}^* = (u^*, v^*)$ in the form:

$$\mathbf{E}_1^* \equiv (0,0), \qquad \mathbf{E}_2^* \equiv (1,1), \qquad \mathbf{E}_3^* \equiv \left(\frac{b}{a-1}, \frac{b}{a-1}\right), \tag{3}$$

with the latter being admissible only for $a > 1$. As can be noticed, all the steady states are characterized by the same concentration of corrosive and passivating, resulting from the intersection of u– and v– nullclines obtained from the equations $f(u, v) = 0$ and $g(u, v) = 0$ respectively, as depicted in Fig. 1.

The local stability properties are established by evaluating the Jacobian matrix at the equilibria:

$$J\left(\mathbf{E}^*\right) = \begin{pmatrix} f_u^* & f_v^* \\ g_u^* & g_v^* \end{pmatrix}, \tag{4}$$

where the subscripts denote the partial derivatives with respect to the indicated variable and the asterisks indicate that the functions are evaluated at $\mathbf{E}^*$. As well known, an equilibrium is locally asymptotically stable with respect to homogeneous perturbations if and only if $\mathrm{tr}\left(J\left(\mathbf{E}^*\right)\right) < 0$ and $\det\left(J\left(\mathbf{E}^*\right)\right) > 0$.

By computing the partial derivatives:

$$\begin{aligned} f_u^*\left(\mathbf{E}_1^*\right) &= -\frac{b}{\delta a}, \quad f_v^*\left(\mathbf{E}_1^*\right) = 0, \\ f_u^*\left(\mathbf{E}_2^*\right) &= \frac{1+b-a}{\delta a}, \quad f_v^*\left(\mathbf{E}_2^*\right) = 0, \\ f_u^*\left(\mathbf{E}_3^*\right) &= \frac{b(a-1-b)}{\delta(a-1)^2}, \quad f_v^*\left(\mathbf{E}_3^*\right) = -\frac{b(a-1-b)}{\delta a(a-1)^2}, \\ g_u^*\left(\mathbf{E}_1^*\right) = g_u^*\left(\mathbf{E}_2^*\right) = g_u^*\left(\mathbf{E}_1^*\right) &= 1, \quad g_v^*\left(\mathbf{E}_1^*\right) = g_v^*\left(\mathbf{E}_2^*\right) = g_v^*\left(\mathbf{E}_3^*\right) = -1, \end{aligned} \tag{5}$$

it is possible to summarize the range of model parameters in which each steady state is locally stable under spatially-homogeneous perturbations as follows:

- $\mathbf{E}_1^*$ $\forall a, b \in \mathbb{R}_+$; (6)
- $\mathbf{E}_2^*$ for $a > 1 + b$, $b \in \mathbb{R}_+$; (7)
- $\mathbf{E}_3^*$ for $1 < a < 1 + b$, $b \in \mathbb{R}_+$. (8)

As known in literature [21,27,28], this system may give rise to excitable dynamics for both $a > 1 + b$ (Fig. 1(a)) and $1 < a < 1 + b$ (Fig. 1(b)).

It can also be proved that, in both ranges of parameters, the dynamical system (2) admits positively invariant regions Ω in the phase plane (u, v). In particular, it can be demonstrated the existence of convex, rectangular, regions $[1, \alpha] \times [0, \beta]$ such that, if the initial datum lies in Ω, then the solution $(u(t), v(t))$ lies in Ω for $\forall (u, v) \in \Omega$ and $\forall t > 0$ [39].

Let us first consider the range of parameters $a > 1 + b$ describing the scenario reported in Fig. 1(a). In this case, the following theorem holds.

Theorem 2.1. *Let $\Omega = [1, \alpha] \times [0, \beta]$ be a closed convex set of $\mathbb{R}^2$, where $\alpha, \beta \in \mathbb{R}^+$ satisfy the restriction $1 < \alpha \le \beta \le a(\alpha - 1) + 1$, then Ω is a positively invariant region for the dynamical system (2) when the model parameters fall in the range $a > 1 + b$.*

Proof. Let us consider the rectangular region of the phase plane $\Omega = [1, \alpha] \times [0, \beta]$ characterized by the outer normal unit vectors $\hat{n}_j$, with $j = 1, \dots, 4$, depicted in Fig. 2(a). In order to establish that Ω is a positively invariant region for the dynamical system (2), with reaction terms $\mathbf{R} = (f(u, v), g(u, v))^T$ defined in (1), let us prove that $\langle \mathbf{R}(t; \bar{\mathbf{E}}), \hat{n} \rangle \le 0 \quad \forall t \in \mathbb{R}^+, \bar{\mathbf{E}} \in \partial\Omega, \hat{n} \in \mathcal{N}_\Omega$, under the restriction $1 < \alpha \le \beta \le a(\alpha - 1) + 1$. Here $\langle , \rangle$ denotes the scalar product and $\mathcal{N}_\Omega$ represents the set of all the outer normal unit vectors to the boundaries of the region Ω.

- On the left boundary, $\hat{n}_1 = (-1, 0)^T$ is the outer normal and $\bar{\mathbf{E}} = (1, v)$ and $v \in [0, \beta]$. Thus, $\langle \mathbf{R}(t; \bar{\mathbf{E}}), \hat{n}_1 \rangle = 0$.
- On the upper boundary, $\hat{n}_2 = (0, 1)^T$ is the outer normal and $\bar{\mathbf{E}} = (u, \beta)$ and $u \in [1, \alpha]$. Thus, $\langle \mathbf{R}(t; \bar{\mathbf{E}}), \hat{n}_2 \rangle = u - \beta \le \alpha - \beta \le 0$ for $\beta \ge \alpha$.
- On the right boundary, $\hat{n}_3 = (1, 0)^T$ is the outer normal and $\bar{\mathbf{E}} = (\alpha, v)$ and $v \in [0, \beta]$. Thus, $\langle \mathbf{R}(t; \bar{\mathbf{E}}), \hat{n}_3 \rangle = \frac{\delta^{-1}}{a} \alpha (1 - \alpha)(a\alpha - b - v) \le 0$ which is fulfilled under the restriction $\beta \le a(\alpha - 1) + 1$ being $\beta \ge \alpha > 1$ and $a > 1 + b$.
- On the lower boundary, $\hat{n}_4 = (0, -1)^T$ is the outer normal and $\bar{\mathbf{E}} = (u, 0)$ and $u \in [1, \alpha]$. Thus, $\langle \mathbf{R}(t; \bar{\mathbf{E}}), \hat{n}_4 \rangle = -u \le 0$.

Therefore, Ω is a positively invariant region for the dynamical system (2) for $a > 1 + b$ under the restriction $1 < \alpha \le \beta \le a(\alpha - 1) + 1$. □

On the other hand, for the case $1 < a < 1 + b$, describing the scenario reported in Fig. 1(b), the following theorem holds.

Theorem 2.2. *Let $\Omega = [1, \alpha] \times [0, \beta]$ a closed convex set of $\mathbb{R}^2$, where $\alpha, \beta \in \mathbb{R}^+$ satisfy the restriction $1 < \alpha \le \beta \le \alpha a - b$, then Ω is a positively invariant region for the dynamical system (2) when the model parameters fall in the range $1 < a < 1 + b$.*

Proof. Let us consider the rectangular region of the phase plane $\Omega = [1, \alpha] \times [0, \beta]$ characterized by the outer normal unit vectors $\hat{n}_j$, with

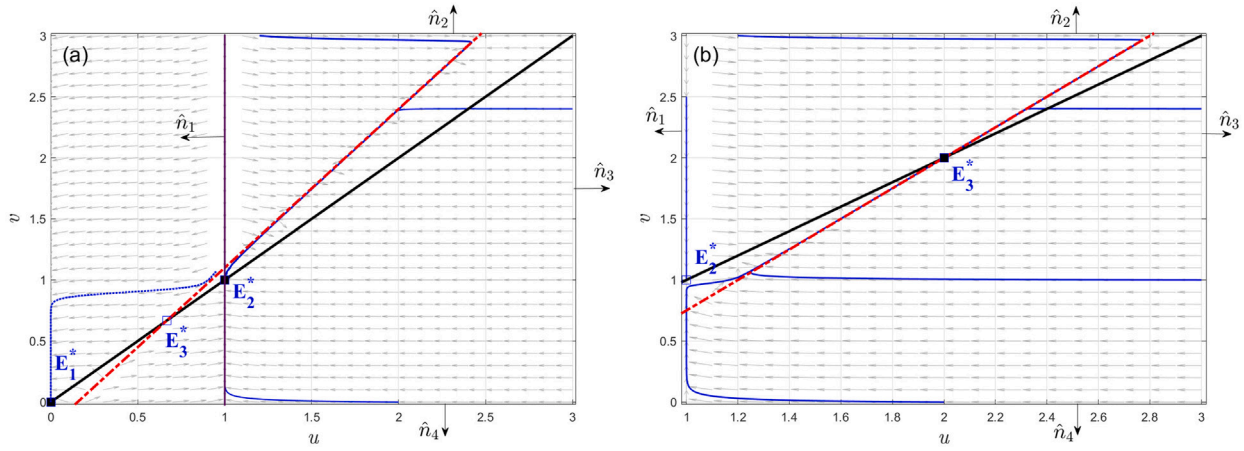

Fig. 2. Phase portraits showing the trajectories of the dynamical system (2) in the (u, v)-plane obtained for different initial conditions (blue lines) in the cases (a) $a > 1 + b$ and (b) $1 < a < 1 + b$. Red dashed–dotted and black solid lines denote the u and v nullclines, as specified in Fig. 1, whereas $\hat{n}_j$ $(j = 1, \dots, 4)$ denote the outer normals to the invariant regions.

$j = 1, \dots, 4$, depicted in Fig. 2(b). By using the same criterion adopted in Theorem 2.1, let us prove that Ω is a positively invariant region for the dynamical system (2), with reaction terms $\mathbf{R} = (f(u, v), g(u, v))^T$ defined in (1), under the restriction $1 < \alpha \leq \beta \leq \alpha a - b$.

- On the left boundary, $\hat{n}_1 = (-1, 0)^T$ is the outer normal and $\bar{\mathbf{E}} = (1, v)$ and $v \in [0, \beta]$. Thus, $\langle \mathbf{R}(t; \bar{\mathbf{E}}), \hat{n}_1 \rangle = 0$.
- On the upper boundary, $\hat{n}_2 = (0, 1)^T$ is the outer normal and $\bar{\mathbf{E}} = (u, \beta)$ and $u \in [1, \alpha]$. Thus, $\langle \mathbf{R}(t; \bar{\mathbf{E}}), \hat{n}_2 \rangle = u - \beta \leq \alpha - \beta \leq 0$ for $\beta \geq \alpha$.
- On the right boundary, $\hat{n}_3 = (1, 0)^T$ is the outer normal and $\bar{\mathbf{E}} = (\alpha, v)$ and $v \in [0, \beta]$. Thus, $\langle \mathbf{R}(t; \bar{\mathbf{E}}), \hat{n}_3 \rangle = \frac{\delta^{-1}}{a} \alpha (1 - \alpha)(a\alpha - b - v) \leq 0$ which is fulfilled under the restriction $\beta \leq \alpha a - b$ being $\beta \geq \alpha > 1$ and $1 < a < 1 + b$.
- On the lower boundary, $\hat{n}_4 = (0, -1)^T$ is the outer normal and $\bar{\mathbf{E}} = (u, 0)$ and $u \in [1, \alpha]$. Thus, $\langle \mathbf{R}(t; \bar{\mathbf{E}}), \hat{n}_4 \rangle = -u \leq 0$.

Therefore, Ω is a positively invariant region for the dynamical system (2) for $1 < a < 1 + b$ under the restriction $1 < \alpha \leq \beta \leq \alpha a - b$. □

A further validation of the above Theorems is also achieved by computing numerically the phase portraits, as depicted in Fig. 2. As can be noticed, any trajectory starting from an initial datum lying in Ω remains indeed in this region $\forall t > 0$ (see solid blue lines). However, the two cases exhibit different behaviours with respect to the stable equilibria. Indeed, for $a > 1 + b$, since $\mathbf{E}_2^*$ lies on the boundary of the invariant region Ω, small perturbations around this state may originate trajectories that move away from this equilibrium (as revealed by the trajectory depicted by the blue dotted line in Fig. 2(a)). On the contrary, for $1 < a < 1 + b$, the equilibrium $\mathbf{E}_3^*$ is localized in the inner part of Ω and any small perturbation around it gives rise to a trajectory entirely contained in Ω.

Considering the goal of establishing the conditions under which these steady states can be destabilized by nonhomogeneous spatial disturbances, no further studies on the equilibrium $\mathbf{E}_1^*$ will be carried out. Indeed, oscillations about this state would lead to negative, and thus nonphysical, values of concentrations.

Moreover, the hypothesis of assuming a non-diffusive character for the passivating species prevents the possibility of observing Turing patterns about $\mathbf{E}_2^*$ and $\mathbf{E}_3^*$ [19]. This suggests the need to generalize model (1) by allowing this species to diffuse too. However, it can be checked that the introduction of standard diffusion for the passivating species does not guarantee the onset of Turing instability. Indeed, the conditions for the stability of the equilibria under homogeneous perturbations and for instability under non-homogeneous ones are never simultaneously met. For this reason, the initiation of pitting corrosion patterns requires additional and different phenomena to be taken into account. A more rigorous description of the phenomena occurring on a metal surface may be achieved by considering the action that the corrosive species plays against the passivating at the mesoscopic level. This is the subject discussed in the next Section.

3. Derivation of the extended Barkley model via fast-reaction limit

The goal of this section is to obtain a macroscopic model of corrosion as the fast-reaction limit of a model valid at the mesoscale, which is built by exploiting the dichotomy of different states and time-scale arguments. As in Section 2, a sufficiently regular spatial domain $\Xi \subset \mathbb{R}^n$, $n = 1, 2$, is considered. The state variables consist of the surface concentration of the corrosive species $u = u(x, t)$ (where $x \in \Xi$ and $t > 0$), and $v = v(x, t)$ mimicking the surface concentration of the recovery species, playing the role of passivating. At the mesoscopic scale, two states for the passivating species may be considered: the pure *passive* state and the *passive film breakdown*, or *pitting*, state. The concentrations of these variables are denoted by $v_P = v_P(x, t)$ and $v_B = v_B(x, t)$, respectively, and are such that $v_P + v_B = v$.

From the chemical viewpoint, such a dichotomy is justified by the fact that oxide film growth on the metal surface provides a passivating action until the oxide film is stable. Corrosive species, such as chloride ions, can adsorb on the oxide film, leading to instability and locally causing film breakdown and pitting corrosion [40].

While the main reactions are described by the Barkley model, it is reasonable to consider a possible switch between passive and breakdown (pitting) states: the passivating in the pure passive state can switch to the breakdown state if the corrosive species is present, while the passivating species (oxide film) in the breakdown (pitting) state can return to the passive state if the corrosive species concentration is low. The corrosive-dependent transition rates are denoted by $h = h(u)$ and $k = k(u)$. In detail, for their chemical meaning, we assume that h is an increasing function of u, while k is a decreasing function of u.

The Point Defect Model (PDM) offers a theoretical framework for understanding how passive films grow and break down, trying to explain the mechanism of pitting corrosion [41]. The PDM suggests that the protective barrier layer of a passive film can be understood by considering how defects (like cation vacancies) are created and destroyed at two key locations: the interface between the metal and the barrier layer, and the interface between the barrier layer and the surrounding solution. When an anion (such as chloride ions) is absorbed into an oxygen vacancy on the surface, the film can react in some ways. One significant response is the creation of cation vacancy/oxygen vacancy pairs through a process similar to a Schottky defect. These

new oxygen vacancies then react with more anions at the film/solution interface, leading to the generation of even more cation vacancies. The generation of these cation vacancies is a self-accelerating (autocatalytic) process. However, whether the film breaks down or not depends on a delicate balance: the rate at which these cation vacancies move across the barrier layer versus the rate at which they are eliminated by metal cations moving from the metal into the film. If the film cannot eliminate the arriving cation vacancies fast enough, these excess vacancies will accumulate. This accumulation causes the film to detach from the underlying metal, leading to localized breakdown and pitting corrosion.

For the above reasons, it can be assumed that the diffusion coefficient of the passive state (oxide film growth) is greater than that one of the pitting state (film oxide breakdown). In particular, denoting by D_P the diffusion coefficient of the passive state of the passivating species, the diffusion coefficient of the pitting state is then $D_B = D_P - \sigma$, $0 \le \sigma \le D_P$.

With these assumptions, the fast-reaction system writes

$$\begin{cases} \partial_t u = D_{11}\Delta u + \delta^{-1} u(1-u)\left(u - \dfrac{v+b}{a}\right), & x \in \Omega,\ t > 0, \\ \partial_t v_P = D_P \Delta v_P + u - v_A - \dfrac{1}{\varepsilon}\left(h(u)v_P - k(u)v_B\right), & x \in \Omega,\ t > 0, \\ \partial_t v_B = (D_P - \sigma)\Delta v_B - v_B + \dfrac{1}{\varepsilon}\left(h(u)v_P - k(u)v_B\right), & x \in \Omega,\ t > 0, \end{cases} \tag{9}$$

together with homogeneous Neumann boundary conditions and nonnegative initial conditions, respectively given by

$$\begin{aligned} &\partial_{\hat n} u(x,t) = \partial_{\hat n} v_P(x,t) = \partial_{\hat n} v_B = 0, && x \in \partial\Omega,\ t > 0, \\ &u(x,0) = u^0(x), \quad v_P(x,0) = v_P^0(x), \quad v_B(x,0) = v_B^0(x), && x \in \Omega, \end{aligned} \tag{10}$$

being $\hat n$ the outer normal vector to the boundary of Ω and Δ the Laplace operator.

It is also assumed that the switching between passive and pitting states happens on a faster time scale, modelled by the time-scale parameter $\varepsilon \ll 1$, and reaches a quasi-steady state at the *macroscopic* level, namely, $h(u)v_P - k(u)v_B = 0$. Since $v = v_P + v_B$, it is possible to express v_P and v_B in terms of u, v and of the transition rates $h(u)$, $k(u)$, obtaining

$$v_P = \frac{k(u)}{h(u)+k(u)}v, \qquad v_B = \frac{h(u)}{h(u)+k(u)}v. \tag{11}$$

Summing the equations for v_P and v_B in Eq. (9), an equation for the passivating species v is deduced, formally reducing the fast-reaction system (9) to a two-species limiting system. In detail, denoting

$$\theta(u) := \frac{h(u)}{h(u)+k(u)}, \tag{12}$$

the limiting system reads

$$\begin{cases} \dfrac{\partial u}{\partial t} = \delta^{-1} u(1-u)\left(u - \dfrac{v+b}{a}\right) + D_{11}\Delta u, \\ \dfrac{\partial v}{\partial t} = u - v + \Delta(D_P v - \sigma\theta(u)v). \end{cases} \tag{13}$$

Thus, the cross-diffusion term appears in the limiting system and incorporates the dichotomy between passive and pitting states on a faster time scale. The cross-diffusion effects depend on the function θ, which is determined by the transition rates describing the switch between the pure passive and the pitting states.

Since in this paper we mainly focus on the possibility of initiating corrosive patterns, we replace the function $\theta(u)$ with a simpler form, namely, we assume $\theta(u) = u$. Denoting

$$D_{11} > 0, \quad D_{22} = D_P > 0, \quad \theta(u) = u, \quad D_{21} = -\sigma < 0,$$

the governing two-species system can be recast in a simpler version as follows:

$$\begin{cases} \dfrac{\partial u}{\partial t} = \delta^{-1} u(1-u)\left(u - \dfrac{v+b}{a}\right) + D_{11}\Delta u, \\ \dfrac{\partial v}{\partial t} = u - v + \Delta(D_{22} v + D_{21} u v), \end{cases} \tag{14}$$

supplemented with homogeneous Neumann boundary conditions and initial conditions.

Remarks. The derivation of the cross-diffusion model is only formal, since the rigorous study of the fast-reaction system and its fast-reaction limit goes beyond the focus of this paper. The transition rates h, k must be nonnegative functions of u, and, due to the structure of the reaction part, the transition rates used for the triangular SKT model [35] might not be suitable for this case.

Model (14) thus represents an extended version of a corrosive-passivating model where the passivating species, assumed to be diffusionless in the original model (1), undergoes both standard (with strength D_{22}) and cross (with strength D_{21}) diffusion effects. The role of these contributions on the excitation of corrosion patterns will be elucidated in the next Section.

4. Turing stability analysis

The goal of this section is to investigate the possible instability of the homogeneous steady states to spatial perturbations. Let us recast the extended model (14) as:

$$\underbrace{\frac{\partial}{\partial t}\begin{pmatrix} u \\ v \end{pmatrix}}_{\mathbf{E}} = \underbrace{\begin{pmatrix} D_{11} & 0 \\ D_{21} v & D_{22} + D_{21} u \end{pmatrix}}_{\mathcal{D}(\mathbf{E})} \begin{pmatrix} \Delta u \\ \Delta v \end{pmatrix} + \underbrace{\begin{pmatrix} 0 \\ 2D_{21} \end{pmatrix}}_{\mathbf{C}} \nabla u \cdot \nabla v + \underbrace{\begin{pmatrix} \delta^{-1} u(1-u)\left(u - \frac{v+b}{a}\right) \\ u - v \end{pmatrix}}_{\mathbf{R}(\mathbf{E})}. \tag{15}$$

As mentioned before, the presence of cross-diffusive terms in a reaction–diffusion system may often lead to the loss of stability of a spatially-homogeneous steady state and the emergence of spatial patterns [38,42]. To inspect the possibility of triggering diffusion-driven instability [43], let us start the analysis by considering the extended model (15) and, after introducing a small perturbation around $\mathbf{E}^\star$ in the form of a simple Fourier mode

$$\mathbf{E} = \mathbf{E}^\star + \mathbf{E}_0 \exp\left(\lambda t + \mathrm{i} k_1 x + k_2 y\right), \tag{16}$$

where λ and $\mathbf{k} = (k_1, k_2)$ represent the growth factor and the wavevector of the perturbation, respectively, the linearized problem can be cast as:

$$\left(\lambda \mathcal{I} - J\left(\mathbf{E}^*\right) + \mathcal{D}^* k^2\right)\mathbf{E}_0 = \mathbf{0}. \tag{17}$$

In (17), k^2 is the square modulus of the wavevector, $\mathcal{D}^* = \mathcal{D}|_{\mathbf{E}=\mathbf{E}^\star}$ while $\mathbf{C}(\nabla u \cdot \nabla v)$ does not contribute in the linearization, being a second-order term.

For the well-posedness of the linearized system [39,44], it must be imposed that $\det(\mathcal{D}^*) > 0$, which implies the restriction:

$$D_{22} + D_{21} u^\star > 0. \tag{18}$$

By expanding the characteristic Eq. (17), it follows that

$$\lambda^2 - \lambda\,\hat m(k^2) + \hat h(k^2) = 0, \tag{19}$$

where

$$\hat m(k^2) = \mathrm{tr}\left(J\left(\mathbf{E}^*\right)\right) - k^2(D_{11} + D_{22} + D_{21} u^\star), \tag{20a}$$

$$\hat h(k^2) = \det\left(\mathcal{D}^*\right) k^4 - q\,k^2 + \det\left(J\left(\mathbf{E}^*\right)\right), \tag{20b}$$

being $q = (D_{22} + D_{21}u^\star)f_u^* + D_{11}g_v^* - D_{21}v^\star f_v^*$.

Keeping in mind condition (18) and that $D_{11} > 0$, together with the condition $\mathrm{tr}\left(J\left(\mathbf{E}^*\right)\right) < 0$ for the stability of the equilibria under homogeneous perturbations, from (20a), it immediately follows that $\hat{m}(k^2) < 0$ for any value of model parameters and wavenumber. Therefore, the stability of the equilibria under non-homogeneous perturbations is only determined by the sign of the function $\hat{h}(k^2)$ defined in (20b). Since it is required that $\det(D^*) > 0$ and $\det\left(J\left(\mathbf{E}^*\right)\right) > 0$, the characteristic Eq. (19) admits eigenvalues with negative real part for any wavenumber k, and thus the corresponding equilibria are locally stable with respect to homogeneous and non-homogeneous perturbations, if and only if the following conditions

$$\begin{cases} \det\left(D^*\right) > 0, \\ \mathrm{tr}\left(J\left(\mathbf{E}^*\right)\right) < 0, \\ \det\left(J\left(\mathbf{E}^*\right)\right) > 0, \\ q^2 - 4\det(D^*)\det\left(J\left(\mathbf{E}^*\right)\right) < 0, \end{cases} \tag{21}$$

are fulfilled. By using (4), (5) and the definitions of D^* and q given above, the previous set of restrictions become:

$$\begin{cases} D_{22} + D_{21}u^\star > 0, \\ f_u^* + g_v^* < 0, \\ f_u^* g_v^* - f_v^* g_u^* > 0, \\ [f_u^*\left(D_{22} + D_{21}u^*\right) - g_v^* D_{11}]^2 + f_v^* D_{21} v^* \left(f_v^* D_{21} v^* - 2g_v^* D_{11}\right) + \\ - 2f_v^*\left(D_{22} + D_{21}u^*\right)\left(f_u^* D_{21} v^* - 2g_u^* D_{11}\right) < 0. \end{cases} \tag{22}$$

In order to destabilize the homogeneous steady state, it is required that $\mathrm{Re}\lambda(k) > 0$ for some $k > 0$. By inspecting (19) and (20b), the only possibility for this to occur is that the function $\hat{h}(k^2) < 0$, which, in turn, requires $q > 0$. This latter inequality is necessary but not sufficient for $\mathrm{Re}\lambda > 0$. Indeed, as is known, the onset of Turing instability is associated with the presence of a null eigenvalue in the characteristic Eq. (19) for a non-null value of wavenumber. In addition, as a control parameter is varied, the transition of $\mathrm{Re}\lambda > 0$ from negative to positive should occur via a maximum (or, equivalently, the transition of $\hat{h}(k^2)$ from positive to negative via a minimum) [19]. In the following analyses, let us consider the cross-diffusion coefficient of the passivating species D_{21} as the main control parameter. The critical values of the control parameter and wavenumber at which such a transition occurs are denoted by D_{21T} and k_T, respectively.

By applying the above definitions, it can be easily checked that the locus of Turing instability (that also implicitly defines D_{21T}) and the critical Turing wavenumber k_T are, respectively, defined as follows:

$$\begin{cases} [f_u^*\left(D_{22} + D_{21}u^*\right) - g_v^* D_{11}]^2 + f_v^* D_{21} v^* \left(f_v^* D_{21} v^* - 2g_v^* D_{11}\right) + \\ - 2f_v^*\left(D_{22} + D_{21}u^*\right)\left(f_u^* D_{21} v^* - 2g_u^* D_{11}\right) = 0, \\ k_T^2 = \left.\dfrac{(D_{22} + D_{21}u^\star)f_u^* + D_{11}g_v^* - D_{21}v^\star f_v^*}{2\,D_{11}\left(D_{22} + D_{21}u^*\right)}\right|_{D_{21}=D_{21T}}, \end{cases} \tag{23}$$

under the restriction $q > 0$.

The obtained conditions are general. In the next subsections, let us study in detail the possibility of generating corrosion patterns around the steady-states $\mathbf{E}_2^*$ and $\mathbf{E}_3^*$.

4.1. Turing patterns about $\mathbf{E}_2^*$

As far as the equilibrium $\mathbf{E}_2^* = (1, 1)$ is concerned, by using (5) and taking into account the restrictions (7) and (18), it is possible to immediately notice that:

$$q = (D_{22} + D_{21})\frac{1 + b - a}{\delta\, a} - D_{11} < 0, \tag{24}$$

so that the function $\hat{h}(k^2) > 0$ and the eigenvalues keep negative real part. This implies that no diffusion-driven instability can be generated about this steady state.

4.2. Turing patterns about $\mathbf{E}_3^*$

As far as the equilibrium $\mathbf{E}_3^* = (b/(a-1), b/(a-1))$ is concerned, by using (5) together with the restrictions (8) and (18), it is possible to conclude that:

$$q > 0 \quad \rightarrow \quad D_{21} < -\frac{a(a-1)\left[bD_{22}(1 + b - a) + (a-1)^2 D_{11}\delta\right]}{b^2(a+1)(1+b-a)} = \widetilde{D}_{21} < 0. \tag{25}$$

Therefore, a necessary condition for Turing instability to occur is that the cross-diffusion coefficient must be negative, in line with its chemical meaning and the analysis carried out in Section 3. On the other hand, the well-posedness condition (18) gives a lower bound for the control parameter:

$$D_{21} > -\frac{D_{22}(a-1)}{b} = \hat{D}_{21} \tag{26}$$

The locus of Turing instability $(23)_1$ takes now the form:

$$D_{21T} = \frac{-\gamma_1 - \sqrt{\gamma_1^2 - 4\gamma_0\gamma_2}}{2\gamma_2} \tag{27}$$

where

$$\begin{aligned} \gamma_2 =& b^4(a+1)^2(1+b-a)^2 \\ \gamma_1 =& 2ab^2(1+b-a)\left[bD_{22}(a^2-1)(1+b-a) + \delta D_{11}(3-a)(a-1)^3\right] \\ \gamma_0 =& a(a-1)^2\left[ab^2 D_{22}^2(1+b-a)^2 + 2bD_{11}D_{22}\delta(2-a)(a-1)^2(1+b-a)\right. \\ &\left. + D_{11}^2\delta^2 a(a-1)^4\right] \end{aligned} \tag{28}$$

while the critical wavenumber $(23)_2$ is expressed as:

$$k_T^2 = \frac{-\delta a D_{11}(a-1)^3 - b(1+b-a)[(1+a)bD_{21T} + (a-1)aD_{22}]}{2\delta a D_{11}(a-1)^2[bD_{21T} + (a-1)D_{22}]}. \tag{29}$$

5. Numerical integration of the governing system

To provide a validation of the theoretical predictions carried out in the previous Section, it is necessary to build suitable numerical schemes to numerically integrate the governing system (14) in both 1D and 2D domains.

In the 1D case, numerical integrations make use of a difference-finite scheme introduced in [45] which has been here modified by means of an implicit method for reaction, standard diffusion, and cross-diffusion terms. Neumann boundary conditions are employed to mimic zero-flux conditions at the edges of the domain. Spatial and temporal domains are discretized with a grid spacing Δx and Δt, respectively, and identifying with u_i^n, v_i^n the approximation to the solution $u(x_i, t^n)$, $v(x_i, t^n)$. Moreover, the time derivative is discretized by using a forward Euler, whereas the spatial derivative is discretized by a backward difference. In particular:

- For the standard diffusion,
$$\frac{\partial^2 u(x_i,t^n)}{\partial x^2} \approx \frac{u_{i+1}^{n+1} - 2\,u_i^{n+1} + u_{i-1}^{n+1}}{\Delta x^2}, \quad \frac{\partial^2 v(x_i,t^n)}{\partial x^2} \approx \frac{v_{i+1}^{n+1} - 2\,v_i^{n+1} + v_{i-1}^{n+1}}{\Delta x^2};$$
- for the cross diffusion,
$$\frac{\partial}{\partial x}\left(\frac{v(x_i,t^n)\partial u(x_i,t^n)}{\partial x}\right) \approx \frac{v_{i+1/2}^{n+1}(u_{i+1}^{n+1} - u_i^{n+1}) - v_{i-1/2}^{n+1}(u_i^{n+1} - u_{i-1}^{n+1})}{\Delta x^2},$$
$$\frac{\partial}{\partial x}\left(\frac{u(x_i,t^n)\partial v(x_i,t^n)}{\partial x}\right) \approx \frac{u_{i+1/2}^{n+1}(v_{i+1}^{n+1} - v_i^{n+1}) - u_{i-1/2}^{n+1}(v_i^{n+1} - v_{i-1}^{n+1})}{\Delta x^2};$$
- for the nonlinear source terms,
$$f(u,v) \approx f(u_i^{n+1}, v_i^{n+1}),\ g(u,v) \approx g(u_i^{n+1}, v_i^{n+1}).$$

After discretization, the system is recast as follows

$$\frac{u_i^{n+1}-u_i^n}{\Delta t} = f(u_i^{n+1},v_i^{n+1}) + D_{11}\left(\frac{u_{i+1}^{n+1}-2\,u_i^{n+1}+u_{i-1}^{n+1}}{\Delta x^2}\right),$$
$$\frac{v_i^{n+1}-v_i^n}{\Delta t} = g(u_i^{n+1},v_i^{n+1}) + D_{22}\left(\frac{v_{i+1}^{n+1}-2\,v_i^{n+1}+v_{i-1}^{n+1}}{\Delta x^2}\right),$$
$$+\ D_{21}\left(\frac{v_{i+1/2}^{n+1}(u_{i+1}^{n+1}-u_i^{n+1}) - v_{i-1/2}^{n+1}(u_i^{n+1}-u_{i-1}^{n+1})}{2\Delta x^2}\right.$$
$$\left.+\ \frac{u_{i+1/2}^{n+1}(v_{i+1}^{n+1}-v_i^{n+1}) - u_{i-1/2}^{n+1}(v_i^{n+1}-v_{i-1}^{n+1})}{2\Delta x^2}\right).$$

To solve the nonlinear system at each time step by adopting the fully implicit discretization described above, the Newton method used in [46,47] is employed.

Let us denote by $\mathbf{E} = [u_1^{n+1},\dots,u_N^{n+1},v_1^{n+1},\dots,v_N^{n+1}]^T \in \mathbb{R}^{2N}$ the vector of unknowns at time t^{n+1}. The discretized equations define a nonlinear system in the form

$$\mathcal{R}(\mathbf{E}) = 0,$$

where $\mathcal{R}(\mathbf{E})$ is the residual vector constructed from the difference equations for u_i^{n+1} and v_i^{n+1} at each spatial node $i = 1,\dots,N$.

Then, the algorithm proceeds iteratively as follows: given an initial guess $\mathbf{E}^{(0)}$, for $l = 0,1,2,\dots$, the corrections $\delta\mathbf{E}^{(l)}$ are computed by solving the linear system

$$\mathcal{J}(\mathbf{E}^{(l)})\delta\mathbf{E}^{(l)} = -\mathcal{R}(\mathbf{E}^{(l)}), \qquad \mathbf{E}^{(l+1)} = \mathbf{E}^{(l)} + \delta\mathbf{E}^{(l)},$$

where $\mathcal{J}(\mathbf{E}^{(l)})$ is the Jacobian matrix of $\mathcal{R}$ evaluated at $\mathbf{E}^{(l)}$.

The Jacobian matrix $\mathcal{J}$ exhibits a sparse block structure, with contributions from the standard diffusion terms, the cross-diffusion, and the nonlinear reaction terms. In particular, the cross-diffusion terms lead to nonzero off-diagonal blocks that couple the u and v components, and these contributions are computed analytically or approximated using numerical differentiation.

Due to the large size and sparsity of $\mathcal{J}$, we employ an iterative Krylov subspace solver for the linear systems at each Newton iteration. In particular, we use the Generalized Minimal Residual method (GMRES) [47], which is well-suited for solving nonsymmetric linear systems. The GMRES method is applied with a suitable stopping criterion, typically based on the norm of the residual of the linear system. To improve convergence, a preconditioner (e.g., ILU or block-diagonal) may be used.

The Newton iterations are stopped when the relative change in the solution satisfies

$$\frac{\|\delta\mathbf{E}^{(l)}\|}{\|\mathbf{E}^{(l)}\|} < \text{tol},$$

for a prescribed tolerance tol (e.g., 10^{-8}).

Boundary conditions (e.g., homogeneous Neumann conditions) are enforced by appropriately modifying both the residual vector and the Jacobian matrix at the boundary nodes. In the case of Neumann conditions, ghost points or modified finite difference formulas are used to ensure consistency and second-order accuracy.

This approach provides a stable and accurate method for computing the fully implicit solution of the reaction–diffusion system with cross-diffusion, even in stiff regimes where explicit schemes would require prohibitively small time steps. In particular, the numerical solutions obtained from this discretization were compared with those provided by `pdepe`, which solves one-dimensional parabolic systems and the explicit discretization used in [45]. The results are more stable than the two methods used to compare them.

In the 2D case, it is possible to employ the same scheme adopted in the 1D case by considering the approximations $u_{i,j}^n, v_{i,j}^n$ of the field variables $u(x_i,y_j,t^n)$, $v(x_i,y_j,t^n)$, together with

- for the linear diffusion terms,

$$\frac{\partial^2 u(x_i,y_j,t^n)}{\partial x^2} \approx \frac{u_{i+1,j}^{n+1}-2\,u_{i,j}^{n+1}+u_{i-1,j}^{n+1}}{\Delta x^2},$$
$$\frac{\partial^2 v(x_i,y_j,t^n)}{\partial x^2} \approx \frac{v_{i+1,j}^{n+1}-2\,v_{i,j}^{n+1}+v_{i-1,j}^{n+1}}{\Delta x^2},$$
$$\frac{\partial^2 u(x_i,y_j,t^n)}{\partial y^2} \approx \frac{u_{i,j+1}^{n+1}-2\,u_{i,j}^{n+1}+u_{i,j-1}^{n+1}}{\Delta y^2},$$
$$\frac{\partial^2 v(x_i,y_j,t^n)}{\partial y^2} \approx \frac{v_{i,j+1}^{n+1}-2\,v_{i,j}^{n+1}+v_{i,j-1}^{n+1}}{\Delta y^2};$$

- for the cross diffusion terms,

$$\frac{\partial}{\partial x}\left(\frac{v(x_i,y_j,t^n)\partial u(x_i,y_j,t^n)}{\partial x}\right) \approx \frac{v_{i+1/2,j}^n(u_{i+1,j}^n-u_{i,j}^n) - v_{i-1/2,j}^n(u_{i,j}^n-u_{i-1,j}^n)}{\Delta x^2},$$
$$\frac{\partial}{\partial y}\left(\frac{v(x_i,y_j,t^n)\partial u(x_i,y_j,t^n)}{\partial y}\right) \approx \frac{v_{i,j+1/2}^n(u_{i,j+1}^n-u_{i,j}^n) - v_{i,j-1/2}^n(u_{i,j}^n-u_{i,j-1}^n)}{\Delta y^2},$$
$$\frac{\partial}{\partial x}\left(\frac{u(x_i,y_j,t^n)\partial v(x_i,y_j,t^n)}{\partial x}\right) \approx \frac{u_{i+1/2,j}^n(v_{i+1,j}^n-v_{i,j}^n) - u_{i-1/2,j}^n(v_{i,j}^n-v_{i-1,j}^n)}{\Delta x^2},$$
$$\frac{\partial}{\partial y}\left(\frac{u(x_i,y_j,t^n)\partial v(x_i,y_j,t^n)}{\partial y}\right) \approx \frac{u_{i,j+1/2}^n(v_{i,j+1}^n-v_{i,j}^n) - u_{i,j-1/2}^n(v_{i,j}^n-v_{i,j-1}^n)}{2\Delta y^2};$$

- for the nonlinear source terms,

$$f(u,v) \approx f(u_{i,j}^n, v_{i,j}^n),\ g(u,v) \approx g(u_{i,j}^n, v_{i,j}^n).$$

After discretization, the governing system becomes:

$$\frac{u_{i,j}^{n+1}-u_{i,j}^n}{\Delta t} = f(u_{i,j}^n, v_{i,j}^n)$$
$$+\ D_{11}\left(\frac{u_{i+1,j}^n-2\,u_{i,j}^n+u_{i-1,j}^n}{\Delta x^2} + \frac{u_{i,j+1}^n-2\,u_{i,j}^n+u_{i,j-1}^n}{\Delta y^2}\right),$$
$$\frac{v_{i,j}^{n+1}-v_{i,j}^n}{\Delta t} = g(u_{i,j}^n, v_{i,j}^n)$$
$$+\ D_{22}\left(\frac{v_{i+1,j}^n-2\,v_{i,j}^n+v_{i-1,j}^n}{\Delta x^2} + \frac{v_{i,j+1}^n-2\,v_{i,j}^n+v_{i,j-1}^n}{\Delta y^2}\right)$$
$$+\ D_{21}\left(\frac{v_{i+1/2,j}^n(u_{i+1,j}^n-u_{i,j}^n) - v_{i-1/2,j}^n(u_{i,j}^n-u_{i-1,j}^n)}{2\Delta x^2}\right.$$
$$\left.+\ \frac{v_{i,j+1/2}^n(u_{i,j+1}^n-u_{i,j}^n) - v_{i,j-1/2}^n(u_{i,j}^n-u_{i,j-1}^n)}{\Delta y^2}\right)$$
$$+\ D_{21}\left(\frac{u_{i+1/2,j}^n(v_{i+1,j}^n-v_{i,j}^n) - u_{i-1/2,j}^n(v_{i,j}^n-v_{i-1,j}^n)}{2\Delta x^2}\right.$$
$$\left.+\ \frac{u_{i,j+1/2}^n(v_{i,j+1}^n-v_{i,j}^n) - u_{i,j-1/2}^n(v_{i,j}^n-v_{i,j-1}^n)}{\Delta y^2}\right),$$

whose approximated solution is retrieved by using the same algorithms described in the 1D case.

6. Numerical results

Let us preliminarily build the region in the (a, D_{21}) plane where Turing instability can take place giving rise to the initiation of corrosion patterns. To this aim, let us fix some common parameters ($\delta = 0.02$, $D_{11} = 1$, $b = 0.5$) and choose two different values of the standard diffusion coefficient of the passivating species: (a) $D_{22} = 0.1$ (Fig. 3(a)) and (b) $D_{22} = 0.5$ (Fig. 3(b)). In both figures, the black solid line denotes the locus $D_{21} = \hat{D}_{21}$, above which the linearized system is well-posed (see (26)), the blue dashed–dotted line represents the condition $D_{21} = \tilde{D}_{21}$, below which $q > 0$ (see (25)), whereas the red solid line depicts the Turing locus $D_{21} = D_{21T}$ (see (27)), below which the stable homogeneous steady state $\mathbf{E}_3^*$ is destabilized via spatially non-homogeneous perturbations. The intersection point $(\bar{a}, \bar{D}_{21})$ among all

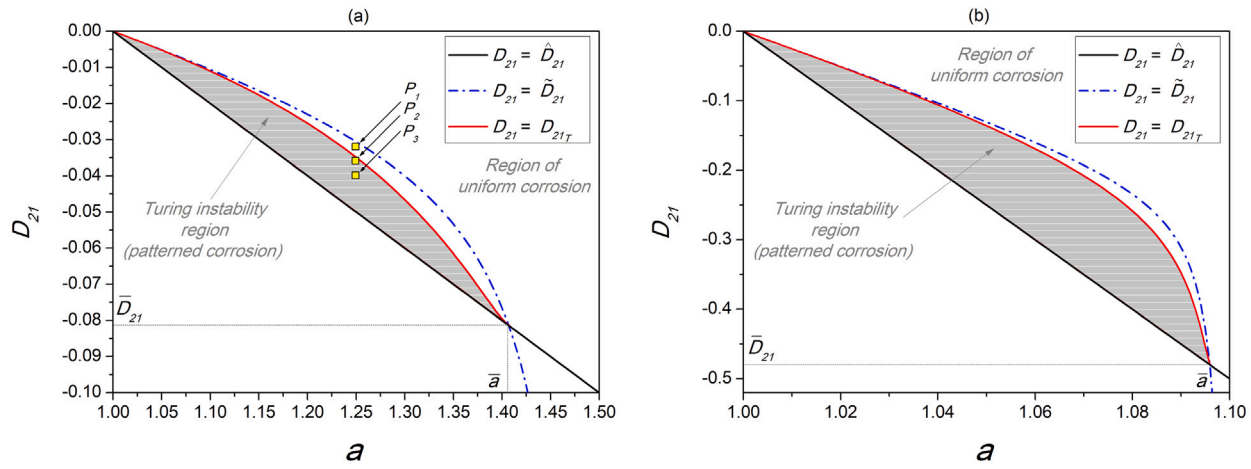

Fig. 3. Turing instability regions in the (a, D_{21}) plane obtained for different values of the standard diffusion coefficient of the passivating species: (a) $D_{22} = 0.1$ and (a) $D_{22} = 0.5$. Common parameters: $\delta = 0.02$, $D_{11} = 1$, $b = 0.5$.

the above loci can be retrieved by the solving the system:

$$\begin{cases} D_{11}\delta\bar{a}^3 - 2D_{11}\delta\bar{a}^2 + (D_{11}\delta + bD_{22})\bar{a} - b(1+b)D_{22} = 0, \\ \bar{D}_{21} = -\dfrac{D_{22}(\bar{a}-1)}{b}. \end{cases} \tag{30}$$

The Turing instability region (shadowed region in the figure) is thus delimited by the loci $\hat{D}_{21}(a)$ and $D_{21T}(a)$, in the range $1 < a < \bar{a}$.

It is interesting to note that the increase in the standard diffusion coefficient D_{22} produces an enlargement of the range of the cross-diffusion coefficient D_{21} but, at the same time, a reduction of the range for a in which Turing patterns can be observed. This result provides a qualitative indication of the possibility of modulating the initiation of corrosion patterns over a fairly wide range of model parameters.

To check the validity of the analytical predictions, let us now consider the points P_i $(i = 1, 2, 3)$ indicated in Fig. 3(a), representative of configurations lying, respectively, outside the Turing region (P_1), within Turing region and close to the instability threshold (P_2), and within Turing region but far from threshold (P_3), and evaluate the wavenumber dependence of the largest eigenvalue of the characteristic Eq. (19). Results reported in Fig. 4 confirm the results of Turing stability analysis. Indeed, at point P_1 $(D_{21} = -0.032$, green dashed–dotted line in the figure), $\mathrm{Re}(\lambda) < 0\,\forall k$, so that the steady state $\mathbf{E}_3^*$ is stable with respect to both homogeneous and nonhomogeneous perturbations, namely, this setup falls into the region of uniform corrosion. By setting the cross-diffusion coefficient at the critical value $D_{21} = D_{21T} = -0.035$, there exists a critical wavenumber $k_T \simeq 5.05$ at which the characteristic Eq. (19) admits a null eigenvalue (solid blue line), in line with the theoretical expectation. By further decreasing the control parameter, at the points P_2 $(D_{21} = -0.036$, dotted red line) and P_3 $(D_{21} = -0.040$, dashed black line), the real part of the eigenvalue becomes positive in the wavenumber range $k_1 < k < k_2$, which denotes the band of unstable modes. The emerging pattern will be thus characterized by a wavenumber which falls into the previous range, compatibly with domain size and boundary conditions [25]. This result also confirms that the possibility of initiating corrosion patterns in the proposed model strictly depends on the strength of cross-diffusion effects. It is indeed required that D_{21} overcomes a given threshold for Turing patterns to emerge.

Theoretical predictions can also be validated by numerical integration of the governing system (14) in both the 1D and 2D domains, as described in Section 5. In particular, in the 1D case, a domain $\Xi = [0, 5]$ has been implemented together with Neumann boundary conditions. Small periodic perturbations of the homogeneous steady state $\mathbf{E}_3^*$ have been used as initial conditions. In all numerical simulations here carried out, it has been checked that the well-posedness condition (18) is fulfilled at every time instant. Using the same set of parameters as in Fig. 4, let us track the spatio-temporal evolution of corrosive and passivating species. As reported in Fig. 5, at the points P_3 (panels on the left) and P_2 (panels in the middle), after a given transient regime, the system develops spatially periodic structures typical of Turing patterns. The amplitude of emerging patterns increases with the distance from the instability threshold (notice the different scales in the colorbars), resembling the typical behaviour of a supercritical instability [23–25]. In contrast, at points P_1 (panels on the right), the initial perturbation expires over time and the system converges towards a stable homogeneous steady state.

Let us now integrate numerically the governing system in a 2D domain. This analysis also has the scope of testing the capability of the proposed model to trigger regular and non-regular corrosion patterns, similar to those observed in real environments. To this aim, let us consider a computational domain $\Xi = [0, 5] \times [0, 5]$ together with Neumann boundary conditions and small periodic perturbations of the homogeneous steady state $\mathbf{E}_3^*$, characterized by different geometries, are used as initial conditions.

The results shown in Figs. 6–8, which depict the asymptotic regimes achieved at the points P_1, P_2, and P_3 at the final computational time window, provide additional confirmations on the validity of theoretical predictions. Indeed, dynamics occurring at point P_1 (Fig. 6) converges towards the uniform corrosion steady-state, so pointing out that this setup lies outside the Turing region. On the contrary, dynamics observed at points P_2 (Fig. 7) and P_3 (Fig. 8) reveal that, depending on the particular choice of the geometry of the perturbation, several regular patterned geometries, such as stripes, spots and hexagons, may be excited. Again, it should be noticed that patterns excited far from the threshold exhibit larger amplitudes. It should be noticed that such regular corrosion patterns have also been observed in experiments [2–6].

As far as non-regular corrosion patterns are considered, in Fig. 9(a,d), two examples of localized corrosion "pits" which typically form in the bottom of fuel tanks and that manifest themselves in the form of isolated or merged holes are reported.

Before addressing a qualitative comparison with such experimental data, it is necessary to preliminarily process the images 9 (a,d) by converting the truecolor format RGB to the greyscale one. Then, the resulting intensity (i.e., the luminance) of each cell $I_{exp}(x, y)$ is normalized with respect to the maximum value, so that $I_{exp}(x, y) \in [0, 1]$. For simplicity, the computational domain is also normalized as $[0, 1]\times[0, 1]$. The resulting maps of experimental intensities are shown in 9 (b,e). To

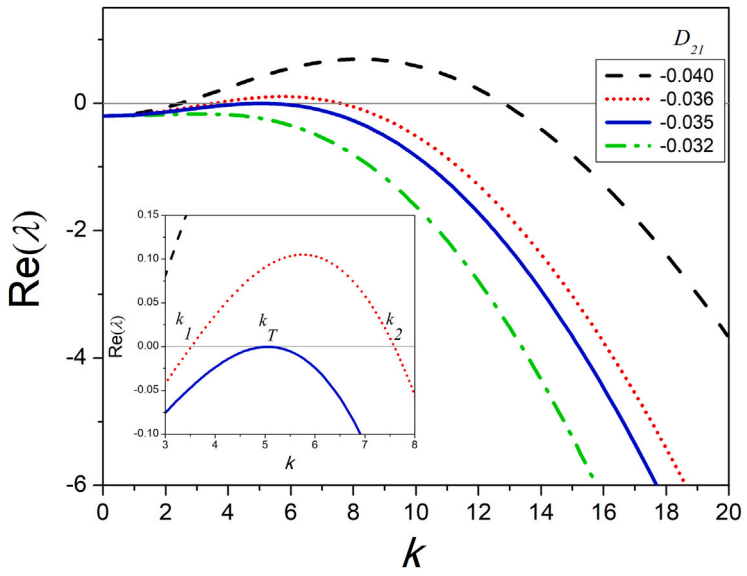

Fig. 4. Real part of the largest eigenvalue λ of the characteristic Eq. (19) as a function of the wavenumber k, for different values of the nonlinear cross diffusion coefficient D_{21}: (green dashed–dotted line) $D_{21} = -0.01$ (point P_1 in Fig. 3), (red solid line) $D_{21} = -0.035$ (point P_2 in Fig. 3), (black dashed line) $D_{21} = -0.04$ (point P_3 in Fig. 3). Common parameters: $\delta = 0.02$, $D_{11} = 1$, $D_{22} = 0.1$, $a = 1.25$, $b = 0.5$.

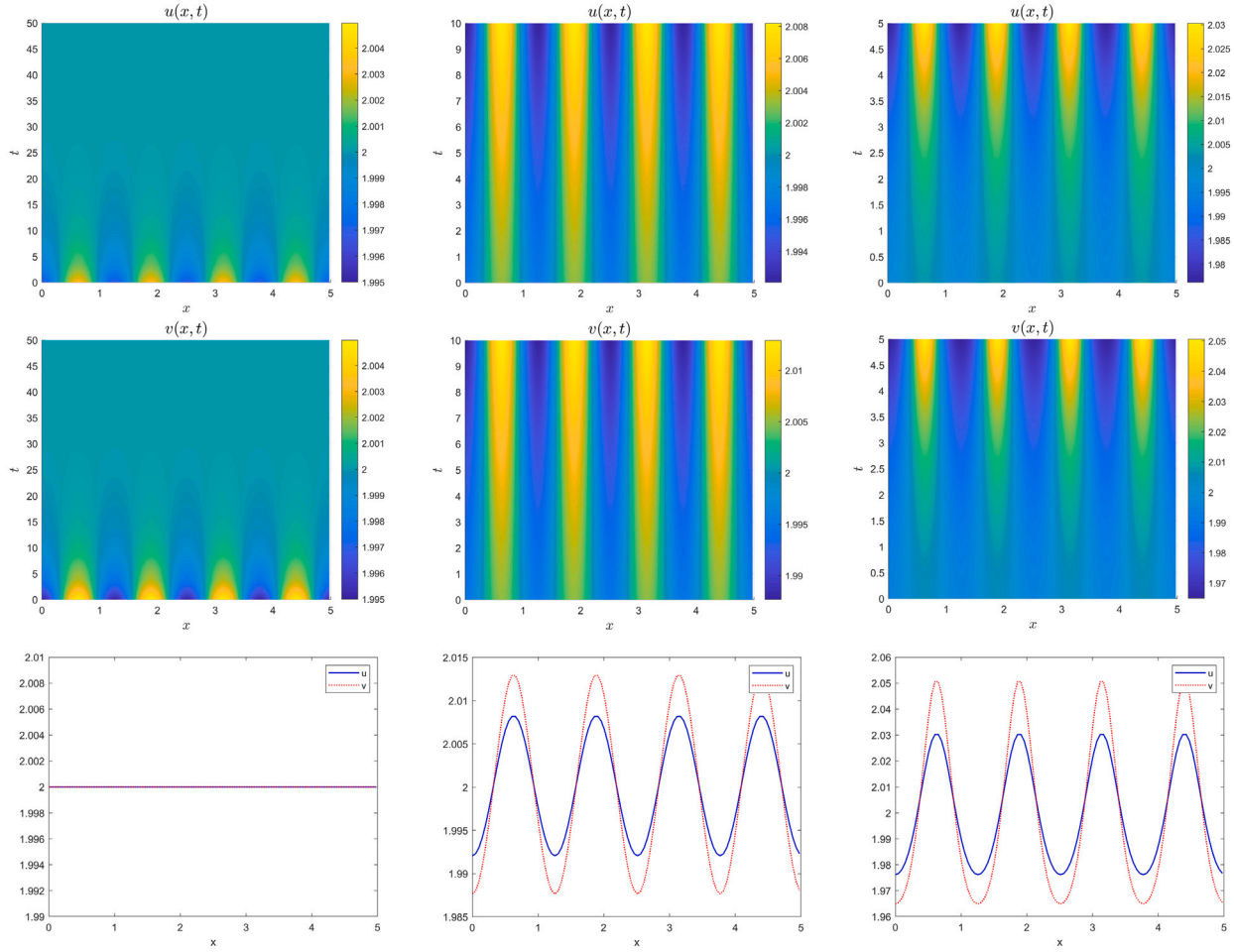

Fig. 5. Numerical integration of the governing system (14) over a 1D domain. (first and second row) Spatio-temporal dynamics of corrosive $u(x,t)$ and passivating $v(x,t)$ species and (last row) the asymptotic regime achieved for the two species, obtained as the control parameter D_{21} is varied. Left, middle and right columns refer to dynamics occurring at P_1 ($D_{21} = -0.032$), P_2 ($D_{21} = -0.036$), and P_3 ($D_{21} = -0.040$), respectively. Common parameters: $\delta = 0.02$, $D_{11} = 1$, $D_{22} = 0.1$, $a = 1.25$, $b = 0.5$.

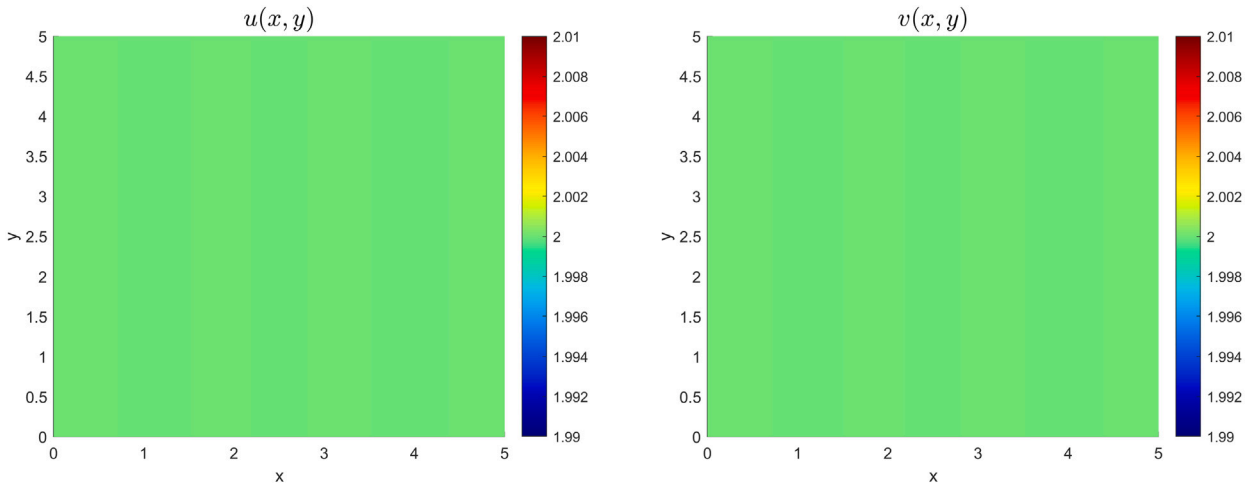

Fig. 6. Numerical integration of the governing system (14) over a 2D domain at the point P_1 depicted in Fig. 3. Panel on the left (right) shows the asymptotic regime of the corrosive (passivating) species.

check whether the proposed model can also support the emergence of non-regular patterns similar to the ones observed experimentally, let us perturb the steady-state $\mathbf{E}_3^*$ via a small random noise, modulated in turn by the intensity map $I_{exp}(x,y)$, and considering the resulting configuration as initial condition for the generalized model (14). The best configuration that allows to qualitatively mimic real corrosion patterns is identified by fixing the parameters $(b, D_{11}, D_{22}, \delta)$, and spanning the couple (a, D_{21}) within the Turing region (depicted in Fig. 3(a)) to minimize the error function ξ

$$\xi = \|I_{num}(x,y) - I_{exp}(x,y)\|_2^2, \tag{31}$$

where $I_{num}(x,y)$ is the intensity map deduced from the rescaling of the corrosion density $u(x,y)$, obtained from numerical simulation, in the range $[0,1]$.

The above analysis provided these best parameter sets: $a = 1.27, D_{21} = -0.04$ for the picture (a) and $a = 1.34, D_{21} = -0.06$ for the one in (d). The resulting asymptotic patterns are reported in panels (c) and (f) of Fig. 9, respectively. The qualitative agreement here obtained suggests that the proposed model captures the most relevant features observed in the experiment. Indeed, it is able to reproduce the initiation of several adjacent pits that merge into some clusters as well as the formation of multiple pits that, despite their proximity, remain isolated and exhibit different corrosion strengths (implying in turn different corrosion depths). This investigation further supports the versatility of the proposed model in triggering a wide range of patterned morphologies, which can be useful to gain deeper insights and hints into the complex process of corrosion of metal surfaces.

7. Conclusions

This manuscript tackled the study of investigating the mechanisms responsible for the initiation of localized corrosion patterns on metal surfaces, such as in the case of the bottom of atmospheric fuel storage tanks. To this aim, the two-compartments Barkley model for corrosive (fast activator) and passivating (slow inhibitor) species was taken into account as a starting point of the present analysis. In its original formulation, the passivating species was assumed to be diffusionless, a hypothesis that prevents the possibility of generating Turing patterns around the spatially-homogeneous steady-states. However, it was proved that, even by relaxing such an assumption and allowing this species to undergo a standard diffusion (with different strength with respect to the corrosive one), the specific functional dependence of the reaction terms still precludes the onset of Turing instability.

To overcome this issue, the complex electrochemical phenomenon of corrosion was inspected at a *mesoscopic* level. Here, the surface concentration of the passivating species may be treated as the sum of two contributions associated with the so-called "passive" and "pitting" states, and the presence of the corrosive species triggers the transition from the former to the latter. By exploiting the above dichotomy and the fast-reaction limit, the resulting model at the *macroscopic* level exhibited a (nonlinear) cross-diffusion term for the passivating species. The extended model so developed allowed us to identify a quite wide region of the parameter space in which corrosion Turing patterns may be observed.

Ad-hoc numerical schemes, which ensured accuracy and stability, were designed to integrate the governing system in both 1D and 2D domains and allowed achieving a twofold aim. On the one hand, they allowed us to corroborate the previous theoretical predictions. On the other hand, they enabled the possibility to mimic, at least qualitatively, real data on localized corrosion that typically arises on metal surfaces. Results confirmed that, if the model parameters fall into the Turing instability region, depending on the choice of initial conditions, the system can evolve into a variety of spatial patterned configurations, ranging from the classical periodic structures in the 1D case to stripes, spots, hexagons and irregular clusters, in the 2D case. This latter observation has, in particular, allowed to reproduce patterns in the form of isolated or merged "pits" that are typically formed in the bottom of fuel tanks and that represent a major hazard due to possible release of pollutants in the environment. All the above findings further confirmed the large potential of the proposed model in improving the existing predictive corrosion tools.

Our results lend themselves to several extensions. For instance, from the modelling perspective, it would be worth considering the possibility of applying, at the same time, dichotomies to both involved species at *mesoscopic* scale to deal with two concurrent cross-diffusion effects at *macroscale*. This generalization is currently under investigation by our research group. From the mathematical viewpoint, the rigorous study of the fast-reaction system and its cross-diffusion limit is essential to establish a solid basis for this study. Furthermore, employing numerical continuation and multiple-scale weakly nonlinear analysis can help to better characterize the different morphologies of corrosion patterns. From the application perspective, it would be interesting to propose a combined model that incorporates the process of pit initiation and pit growth. This would contribute to defining more rigorously the real hazards, quantifying the residual lifetime of fuel tanks, and providing industrial operators with some specific hints for the improvement of risk-based inspection planning.

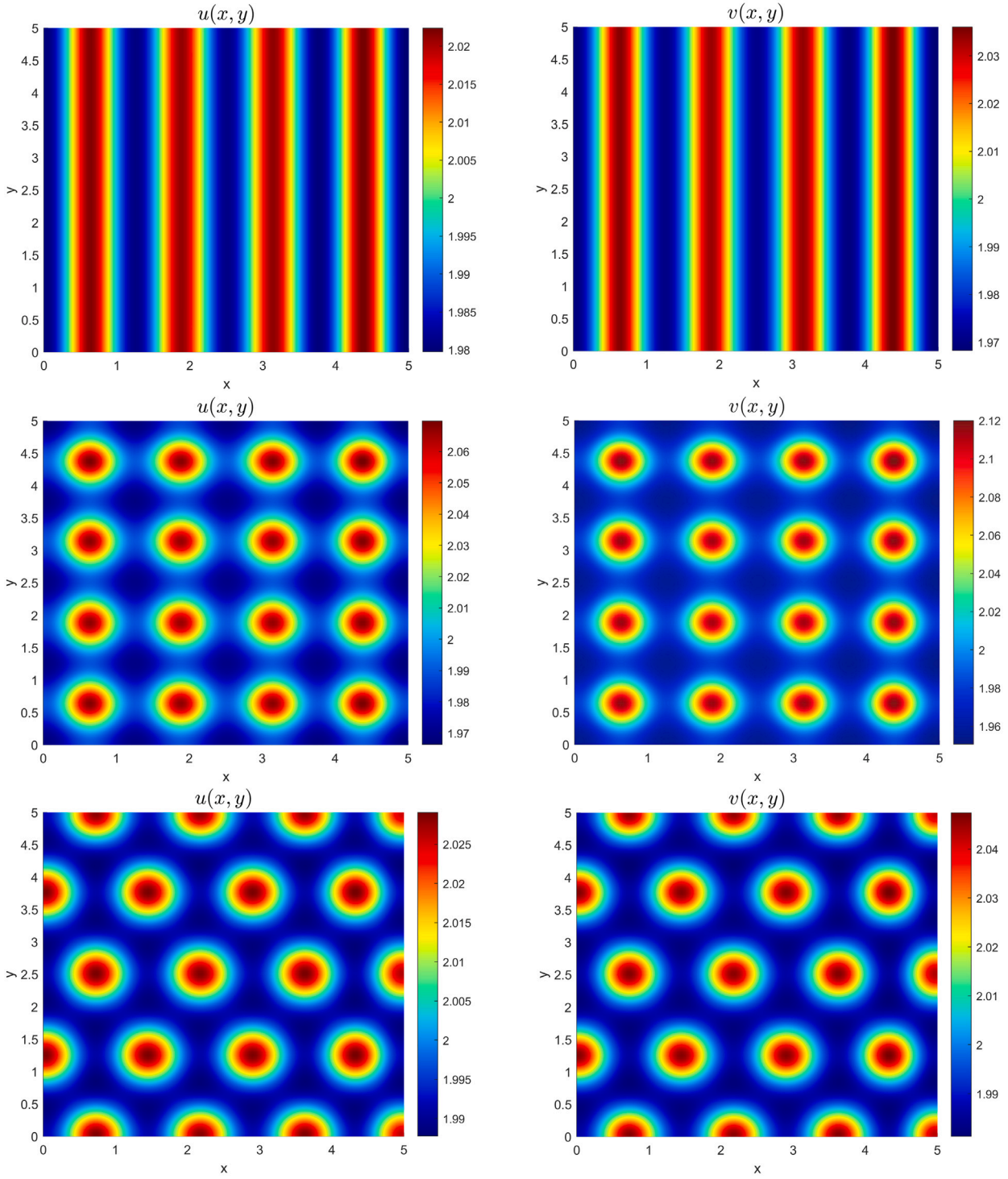

Fig. 7. Numerical integration of the governing system (14) over a 2D domain at the point P_2 depicted in Fig. 3. Panels on the left (right) show the asymptotic regime of the corrosive (passivating) species. Stripes, spots, and hexagons are obtained by using different small periodic perturbations of the steady state $\mathbf{E}_3^*$.

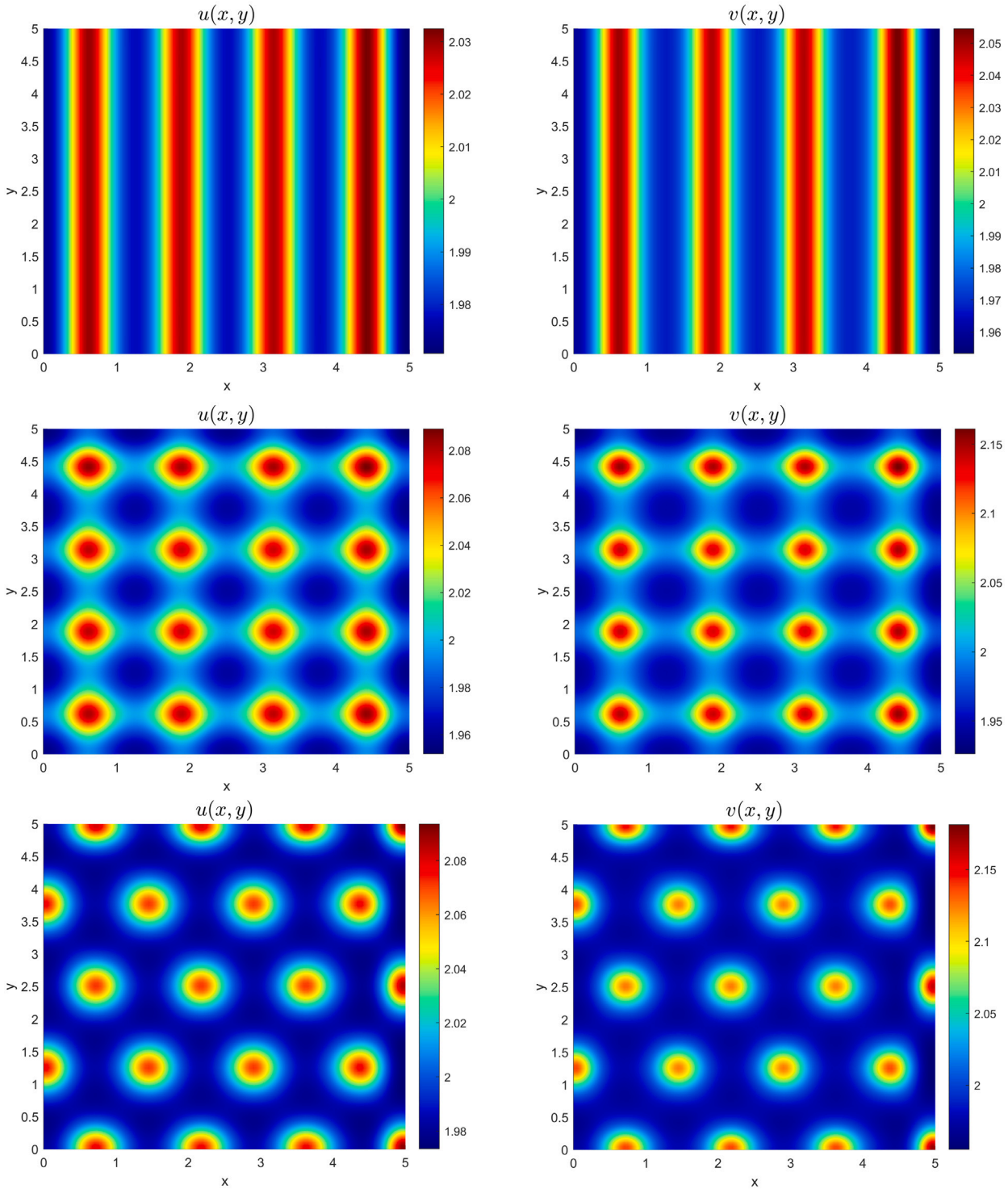

Fig. 8. Numerical integration of the governing system (14) over a 2D domain at the point P_3 depicted in Fig. 3. Panels on the left (right) show the asymptotic regime of the corrosive (passivating) species. Stripes, spots, and hexagons are obtained by using different small periodic perturbations of the steady state $\mathbf{E}_3^*$.

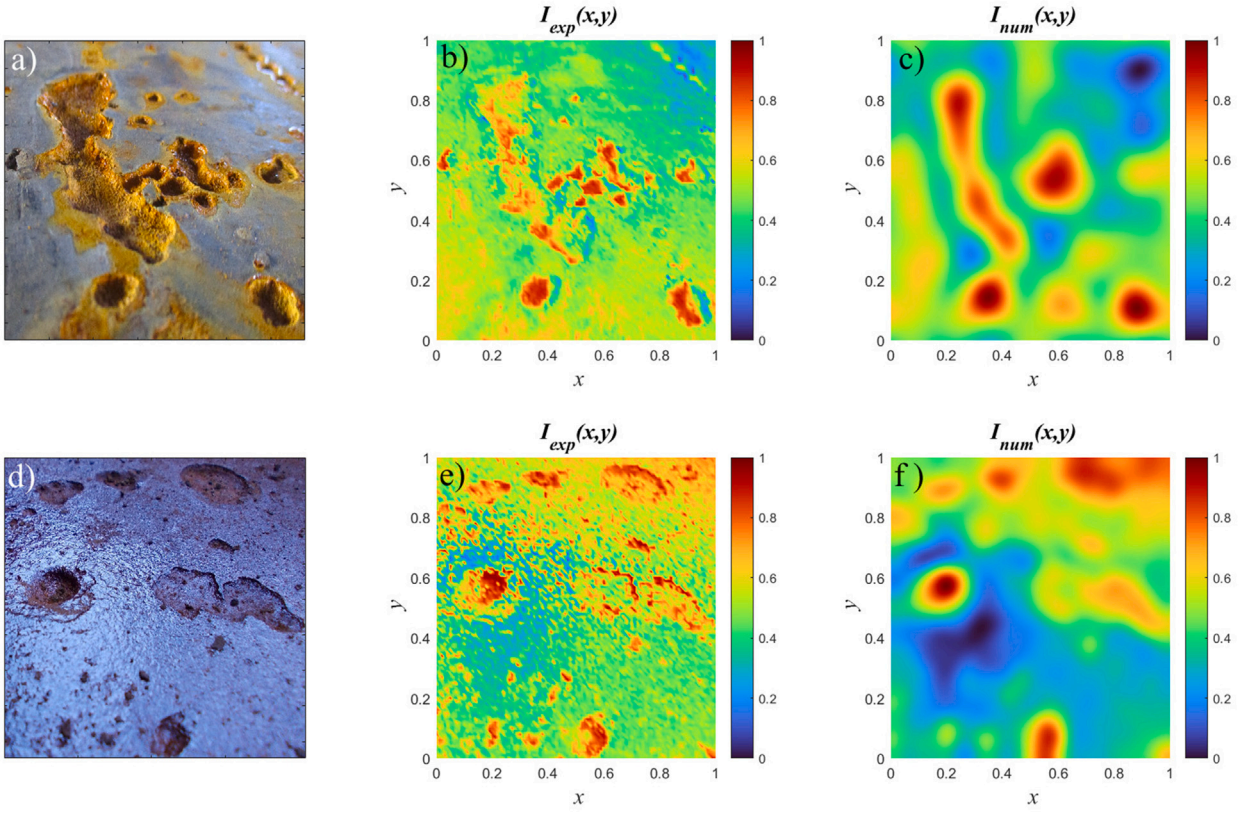

Fig. 9. (a,d) Experimental pictures of real corroded bottoms of fuel tanks and (b,e) the corresponding intensity (luminance) maps $I_{exp}(x, y)$. Panels (c,f) represent the numerically-obtained intensity maps $I_{num}(x, y)$ obtained by suitable normalization of the corrosion density $u(x, y)$ and by minimizing the error function ξ, defined in (31). Parameter sets: (c) $a = 1.27$, $D_{21} = -0.04$; (f) $a = 1.34$, $D_{21} = -0.06$. The other parameters are $b = 0.5$, $D_{11} = 1$, $D_{22} = 0.1$, $\delta = 0.02$ in both cases.

CRediT authorship contribution statement

Giancarlo Consolo: Writing – review & editing, Writing – original draft, Supervision, Software, Methodology, Investigation, Funding acquisition, Formal analysis, Conceptualization. **Guglielmo Inferrera:** Writing – review & editing, Writing – original draft, Software, Methodology, Investigation, Formal analysis. **Edoardo Proverbio:** Writing – review & editing, Writing – original draft, Methodology, Investigation. **Cinzia Soresina:** Writing – review & editing, Writing – original draft, Software, Methodology, Investigation, Formal analysis.

Declaration of competing interest

The authors declare that they have no known competing financial interests or personal relationships that could have appeared to influence the work reported in this paper.

Acknowledgements

GC, GI, and CS are members of the INdAM-GNFM. This research was funded by MUR (Italian Ministry of University and Research) PNRR-Missione 4, Componente 2, Investimento 1.1–Bando Prin 2022, Decreto Direttoriale no. 104 del 02-02-2022, through PRIN2022 Project PRIN_202248TY47 "Modelling complex biOlogical systeMs for biofuEl productioN and sTorAge: mathematics meets green industry (MOMENTA)" CUP J53D23003580006. CS has received funding from the Programma Giovani Ricercatori "Rita Levi Montalcini" 2021.

Data availability

No data was used for the research described in the article.

References

[1] N. Perez, Electrochemical corrosion, in: Electrochemistry and Corrosion Science, Springer International Publishing, Cham, 2016, pp. 1–23, http://dx.doi.org/10.1007/978-3-319-24847-9-1.

[2] V.B. Vukkum, et al., Enhanced corrosion resistance of additively manufactured stainless steel by modification of feedstock, Npj Mater. Degrad. 6.1 (2) (2022) http://dx.doi.org/10.1038/s41529-021-00215-z.

[3] R.A. Leishear, Fluid Mechanics, Water Hammer, Dynamic Stresses, and Piping Design, Asme Press, New York, 2013.

[4] D.A. Shifler, Localized corrosion, in: Corrosion in Marine Environments, John Wiley & Sons, Inc., 2022, pp. 63–121, http://dx.doi.org/10.1002/9781119788867.ch4.

[5] J.R. Galvele, Pitting corrosion, in: J.C. Scully (Ed.), Treatise on Materials Science and Technology, Elsevier, 1983, pp. 1–57, http://dx.doi.org/10.1016/B978-0-12-633670-2.50006-1.

[6] V. Maurice, M. Philippe, Current developments of nanoscale insight into corrosion protection by passive oxide films, Curr. Opin. Solid State Mater. Sci. 22.4 (2018) 156–167, http://dx.doi.org/10.1016/j.cossms.2018.05.004.

[7] H. Moradi, G. Grifò, M.F. Milazzo, E. Proverbio, G. Consolo, Modelling localized corrosion in biofuel storage tanks, Math. Biosc. Eng. 22 (2025) 677–699, http://dx.doi.org/10.3934/mbe.2025025.

[8] L.N. Komariah, S. Arita, B.E. Prianda, T.K. Dewi, Technical assessment of biodiesel storage tank: a corrosion case study, J. King Saud. Univ. Eng. Sci. 35 (2023) 232–237, http://dx.doi.org/10.1016/j.jksues.2021.03.016.

[9] K.A. Zahan, M. Kano, Biodiesel production from palm oil, its by-products, and mill effluent: A review, Energies 11 (2018) 2132, http://dx.doi.org/10.3390/en11082132.

[10] A. Groysman, Corrosion in systems for storage and transportation of petroleum products and biofuels: Identification, in: Monitoring and Solutions, Springer Dordrecht, 2014, http://dx.doi.org/10.1007/978-94-007-7884-9.

[11] API 580 - risk based inspection, 2023, Available from: https://www.api.org/products-andservices/individual-certification-programs/certifications/api580.

[12] M.F. Milazzo, G. Ancione, P. Bragatto, E. Proverbio, A probabilistic approach for the estimation of the residual useful lifetime of atmospheric storage tanks in oil industry, J. Loss Prev. Proc. Ind. 77 (2022) 104781, http://dx.doi.org/10.1016/j.jlp.2022.104781.

[13] C. Cui, R. Ma, E. Martínez-Pañeda, Electro-chemo-mechanical phase field modeling of localized corrosion: theory and COMSOL implementation, Eng. Comput. 39 (2023) 3877–3894, http://dx.doi.org/10.1007/s00366-023-01833-8.
[14] W. Mai, S. Soghrati, R.G. Buchheit, A phase field model for simulating the pitting corrosion, Corros. Sci. 110 (2016) 157–166, http://dx.doi.org/10.1016/j.corsci.2016.04.001.
[15] S.M. Sharland, P.W. Tasker, A mathematical model of crevice and pitting corrosion—I, the physical model, Corros. Sci. 28 (1988) 603–620, http://dx.doi.org/10.1016/0010-938X(88)90027-3.
[16] S.M. Sharland, A mathematical model of crevice and pitting corrosion—II, the mathematical solution, Corros. Sci. 28 (1988) 621–630, http://dx.doi.org/10.1016/0010-938X(88)90028-5.
[17] J. Bhandari, F. Khan, R. Abbassi, V. Garaniya, R. Ojeda, Modelling of pitting corrosion in marine and offshore steel structures – a technical review, J. Loss Prev. Proc. Ind. 37 (2015) 39–62, http://dx.doi.org/10.1016/j.jlp.2015.06.008.
[18] T.Q. Ansari, Z. Xiao, S. Hu, Y. Li, J.L. Luo, S.Q. Shi, Phase-field model of pitting corrosion kinetics in metallic materials, NPJ Comput. Mater. 4 (2018) 38, http://dx.doi.org/10.1038/s41524-018-0089-4.
[19] J.D. Murray, Mathematical biology II, in: Spatial Models and Biomedical Applications, Springer, Berlin, 2003.
[20] J.M. Epstein, Nonlinear Dynamics, Mathematical Biology, and Social Science, Addison-Wesley, Reading, MA, 1997, pp. 97–99.
[21] M. Cross, H. Greenside, Pattern Formation and Dynamics in Nonequilibrium Systems, Cambridge Univ. Press, UK, 2009.
[22] E. Barbera, G. Consolo, G. Valenti, Spread of infectious diseases in a hyperbolic reaction–diffusion susceptible-infected-removed model, Phys. Rev. E 88 (2013) 052719, http://dx.doi.org/10.1103/PhysRevE.88.052719.
[23] G. Consolo, C. Currò, G. Valenti, Supercritical and subcritical turing pattern formation in a hyperbolic vegetation model for flat arid environments, Phys. D 398 (2019) 141–163, http://dx.doi.org/10.1016/j.physd.2019.03.006.
[24] G. Grifó, G. Consolo, C. Curró, G. Valenti, Rhombic and hexagonal pattern formation in 2D hyperbolic reaction–transport systems in the context of dryland ecology, Phys. D 449 (2023) 133745, http://dx.doi.org/10.1016/j.physd.2023.133745.
[25] G. Consolo, C. Curró, G. Grifó, G. Valenti, Vegetation pattern formation and transition in dryland ecosystems with finite soil resources and inertia, Phys. D 476 (2025) 134601, http://dx.doi.org/10.1016/j.physd.2025.134601.
[26] G. Inferrera, C.F. Munafò, F. Oliveri, P. Rogolino, Reaction–diffusion models of crimo–taxis in a street, Appl. Math. Comput. 467 (2024) 128504, http://dx.doi.org/10.1016/j.amc.2023.128504.
[27] D. Barkley, A model for fast computer simulation in excitable media, Phys. D 49 (1991) 61, http://dx.doi.org/10.1016/0167-2789(91)90194-E.
[28] D. Barkley, Euclidean symmetry and the dynamics of rotating spiral waves, Phys. Rev. Lett. 72 (1994) 164, http://dx.doi.org/10.1103/PhysRevLett.72.164.
[29] N. DeTal, A. Kaboudian, F.H. Fenton, Terminating spiral waves with a single designed stimulus, Proc. Natl. Acad. Sci. USA 119 (2022) e2117568119, http://dx.doi.org/10.1073/pnas.2117568119.
[30] K. Gallagher, M.A. Strobl, D.S. Park, F.C. Spoendlin, R.A. Gatenby, P.K. Maini, A.R. Anderson, Mathematical model-driven deep learning enables personalized adaptive therapy, Cancer Res. 84 (2024) 1929, http://dx.doi.org/10.1158/0008-5472.CAN-23-2040.
[31] B.C. Batista, E. Romanovskaia, V. Romanovski, M. Emmanuel, J.T. Burns, J. Ma, I.Z. Kiss, J.R. Scully, O. Steinbock, Morphogenic modeling of corrosion reveals complex effects of intermetallic particles, Adv. Sci. 11 (2024) 2404986, http://dx.doi.org/10.1002/advs.202404986.
[32] L. Desvillettes, C. Soresina, Non-triangular cross-diffusion systems with predator–prey reaction terms, Ric. di Mat. 68 (2019) 295–314, http://dx.doi.org/10.1007/s11587-018-0403-y.
[33] J. Eliaš, D. Hilhorst, M. Mimura, Y. Morita, Singular limit for a reaction–diffusion-ODE system in a neolithic transition model, J. Differential Equations 295 (2021) 39–69, http://dx.doi.org/10.1016/j.jde.2021.05.044.
[34] J. Eliaš, H. Izuhara, M. Mimura, B.Q. Tang, An aggregation model of cockroaches with fast-or-slow motion dichotomy, J. Math. Biol. 85 (2022) 28, http://dx.doi.org/10.1007/s00285-022-01797-1.
[35] M. Iida, M. Mimura, H. Ninomiya. Diffusion, Cross-diffusion and competitive interaction, J. Math. Biol. 53 (2006) 617–641, http://dx.doi.org/10.1007/s00285-006-0013-2.
[36] J. Morgan, C. Soresina, B.Q. Tang, B.N. Tran, Singular limit and convergence rate via projection method in a model for plant-growth dynamics with autotoxicity, J. Differential Equations 452 (2026) 113797, http://dx.doi.org/10.1016/j.jde.2025.113797.
[37] E. Brocchieri, L. Corrias, H. Dietert, Y.-J. Kim, Evolution of dietary diversity and a starvation driven cross-diffusion system as its singular limit, J. Math. Biol. 83 (2021) 1–40, http://dx.doi.org/10.1007/s00285-021-01679-y.
[38] F. Giannino, A. Iuorio, C. Soresina, Beyond water limitation in vegetation–autotoxicity patterning: a cross-diffusion model, 2025, arXiv preprint arXiv:2506.03981.
[39] J. Smoller, Shock Waves and Reaction–Diffusion Equations, second ed., Springer, 1994.
[40] P.M. Natishan, W.E. O'Grady, Chloride ion interactions with oxide-covered aluminum leading to pitting corrosion: a review, J. Electrochem. Soc. 161 (2014) C421, http://dx.doi.org/10.1149/2.1011409jes.
[41] D.D. Macdonald, The point defect model for the passive state, J. Electrochem. Soc. 139 (1992) 3434, http://dx.doi.org/10.1149/1.2069096.
[42] G. Gambino, M.C. Lombardo, M. Sammartino, Pattern formation driven by cross-diffusion in a 2D domain, Nonlinear Anal. Real World Appl. 14.3 (2013) 1755–1779, http://dx.doi.org/10.1016/j.nonrwa.2012.11.009.
[43] A. Turing, The chemical basis of morphogenesis, Philos. Trans. R. Soc. B 237 (1952) 37–72.
[44] D.G. Miller, Some comments on multicomponent diffusion: negative main term diffusion coefficients, second law constraints, solvent choices, and reference frame transformations, J. Phys. Chem. 90 (1986) 1509–1519, http://dx.doi.org/10.1021/j100399a010.
[45] A. Chertock, A. Kurganov, A second-order positivity preserving central-upwind scheme for chemotaxis and haptotaxis models, Numer. Math. 111 (2008) 169–205, http://dx.doi.org/10.1007/s00211-008-0188-0.
[46] R. Ruiz-Baier, C. Tian, Mathematical analysis and numerical simulation of pattern formation under cross-diffusion, Nonlinear Anal. Real World Appl. 14.1 (2013) 601–612, http://dx.doi.org/10.1155/2013/891738.
[47] P. Knabner, L. Angermann, A. Rupp, Numerical Methods for Elliptic and Parabolic Partial Differential Equations, Springer, 2003.